Available online at www.sciencedirect.com
SCIENCE DIRECT®

Journal of Sound and Vibration 293 (2006) 320–334

JOURNAL OF
SOUND AND
VIBRATION

www.elsevier.com/locate/jsvi

Transient waves in a compliant cylindrical cavity enclosing comminuted material

Michael El-Raheb*

ATK Mission Research, Laguna Hills CA, USA

Received 2 July 2004; received in revised form 2 September 2005; accepted 3 October 2005
Available online 11 November 2005

Abstract

An acoustic model is presented for analyzing transient waves from impact on a mass of confined comminuted material. Two approaches are considered: a modal approach utilizing the static-dynamic superposition method, and a finite difference approach. For prescribed motion at the footprint, analysis proceeds by superimposing response from several external annular segments of unit pressure gradient and with time-dependent weights yielding a combined response equal to the prescribed instantaneous motion. Pressure histories from the two approaches are in agreement. The effect on response of prescribed motion parameters and wall mobility is studied.

1. Introduction

In ballistic events of metal projectiles striking ceramic tiles, the shock generated at the interface of projectile and tile yields the projectile and starts the propagation of cracks into the brittle ceramic material. As long as the comminuted ceramic material remains in the path of the eroding projectile, its motion is resisted producing deceleration. As strain energy of broken ceramic is converted to kinetic energy, comminuted ceramic material is propelled parallel and opposite to the projectile motion. This reduces resistance to projectile motion allowing the projectile to penetrate further. It was observed that confining a comminuted ceramic for longer time after crack initiation enhances its stopping ability. One way to confine comminuted material is to encapsulate the ceramic tile in a strong but light thin metallic shell. After cracking, the ceramic is broken into small particles varying in size from powder-like at the projectile's footprint to larger chunks remote from the footprint. In the comminuted state, the ceramic looses its shear strength while maintaining its compressive strength similar to the case of a soil whose only resistance to shear stresses is friction. Consequently, pressure generated by the penetrating projectile can be approximated by a piston with prescribed time-dependent motion acting on a fluid volume confined by compliant boundaries. It is the pressure rise in the sand-like ceramic confined by the capsule that ultimately fails, culminating in ejecta of the broken material and reduction in resistance against projectile penetration. Since the comminuted material is confined by the resilient walls of the capsule, deformations and particle motions are small justifying linear acoustic theory.

---

*Tel.: +1 626 796 5528; fax: +1 626 583 8834.
E-mail address: mertrident@earthlink.net.

0022-460X/$ - see front matter © 2005 Elsevier Ltd. All rights reserved.
doi:10.1016/j.jsv.2005.10.001

Moreover, friction between particles and the inability to resist tension reduce the possibility of shock formation.

To justify the validity of the linear acoustic model in simulating this seemingly nonlinear phenomenon, results of the present linear acoustic analysis with compliant boundaries are compared with results from a nonlinear general-purpose finite difference program "EPIC2". The magnitude of pressure near and remote from the projectile's footprint compare favorably from the two models. In fact, the instantaneous radial dynamic pressure distribution in the capsule from the two models also compares favorably during the event from impact to times when pressure is attenuated almost completely.

This comparison between results of a nonlinear simulation that considers crack initiation and propagation including the interaction between the metallic capsule and the comminuted ceramic, and such an over-simplified linear acoustic model clearly indicates that the nonlinearity during the event is negligible and that a linear acoustic model is sufficiently accurate to simulate the event provided compliance of the capsule's walls are carefully considered.

Acoustic wave propagation governed by the Helmholtz equation has been treated extensively in the literature. Solution techniques range from analytical for simple geometries to numerical for problems with complicated geometry, medium inhomogeniety and nonlinearity. Theil [1] treats the 1-D viscoelastically damped wave equation analytically. Yserentant [2] shows how a consistent discretization of the acoustic equation can be recovered from the particle model of compressible fluids [3]. Sina and Khashayar [4] solve the 3-D wave equation analytically for arbitrary non-homogeneous media adopting the differential transfer matrix. Sujith et al. [5] determine an exact solution to 1-D transient waves in curvilinear coordinates adopting transformation of variables suggested by the WKB approximation. Hamdi et al. [6] present exact solitary wave solutions of the 1-D wave propagation in nonlinear media with dispersion. Yang [7] solves numerically the wave equation with attenuation from linear friction utilizing grid modification to track wave fronts accurately. Narayan [8] solves the 3-D transient acoustics in inhomogeneous media by finite difference and Schemann and Bornemann [9] apply the adaptive Rothe integrator. Bailly and Juve [10] present a numerical solution to the 2-D acoustic propagation from transient sources using the dispersion-relation-preserving scheme in space and a fourth-order Kutta–Runge in time. Wagner et al. [11], and Gaul and Wenzel [12] use a hybrid boundary element method for frequency and transient acoustic response in bounded and unbounded regions. Mehdizadeh and Paraschivoiu [13] develop a spectral element method to solve the 3-D Helmholtz equation retaining accuracy for large wavenumbers. The present work is the first to address analytically the 3-D transient propagation from impact in a confined medium with compliant boundaries.

Section 2 formulates the modal approach. The prescribed pressure gradient at the footprint is treated by the static-dynamic superposition method [14]. Pressure is expressed as a superposition of two solutions; a static solution satisfying inhomogeneous boundary conditions multiplied by the time dependence of the forcing function, and a modal solution satisfying homogeneous boundary conditions. Since the excited face has a mixed boundary condition, a mixed boundary value problem arises. This difficulty can be overcome by the influence method [15].

To confirm results of this modal approach that relies on influence coefficients, comparisons are made to a finite difference solution developed in Appendix A. One advantage of this solution is that mixed boundary conditions are readily included. Section 3 discusses numerical results. Since the modal analysis in Section 2 applies the static-dynamic superposition method to the external excitation, a comparison of the static solutions from the two methods is presented first. This is followed by transient response in a constrained layer.

2. Analysis

The pressure from impact of comminuted material in a flexible cylindrical capsule $\{(r,z),\ 0\leqslant r\leqslant r_d,\ 0\leqslant z\leqslant h\}$ is approximated by the transient acoustic pressure in a compressible fluid disk enclosed in a cavity with compliant boundaries and with time-dependent acceleration applied over a concentric footprint $r\leqslant r_p$. This translates to the boundary conditions

$$\partial_r p(r_d,z;t) + Y_r p(r_d,z;t) = 0, \tag{1a}$$

$$\partial_z p(r,0;t) = \begin{cases} -\rho \ddot{f}_w(t), & 0 \leqslant r \leqslant r_p, \\ Y_z p(r,0;t), & r_p < r \leqslant r_d, \end{cases} \tag{1b}$$

$$\partial_z p(r,h;t) + Y_z p(r,h;t) = 0, \tag{1c}$$

where $p(r,z;t)$ is acoustic pressure, Y_r, Y_z are frequency independent mobilities of the resilient boundaries relating pressure to normal pressure gradient determined in Ref. [16], (r,z) are radial and axial coordinates, ρ is density, (h,r_d) are layer length and radius, r_p is footprint radius, t is time, $\ddot{f}_w(t)$ is prescribed acceleration at the footprint, $(\dot{\ })$ is time derivative, and $H(r)$ is the Heaviside function.

Acoustic propagation in the fluid disk is governed by the acoustic equation

$$(\partial_{rr} + 1/r\partial_r + \partial_{zz} - 1/c_b^2\partial_{tt})p_d = 0 \tag{2}$$

with boundary conditions given by Eq. (1), where z has its origin at the excited boundary. Express $p(r,z;t)$ as a superposition of three terms:

$$p(r,z;t) = -p_s(r,z)\rho\ddot{f}_w(t) + p_d(r,z;t) + p_{s0}f_w(t). \tag{3}$$

$p_d(r,z;t)$ is the dynamic solution satisfying Eq. (2) and the homogeneous boundary conditions (1), and $p_s(r,z)$ is the static solution satisfying

$$\nabla_0^2 p_s = 0 \tag{4a}$$

and the inhomogeneous boundary conditions

$$\begin{aligned} &\partial_r p_s(r_d,z) + Y_r p_s(r_d,z) = 0, \\ &\partial_z p_s(r,0) = \begin{cases} -1, & 0 \leqslant r \leqslant r_p, \\ Y_z p_s(r,0), & r_p < r \leqslant r_d, \end{cases} \\ &\partial_z p_s(r,h) + Y_z p_s(r,h) = 0. \end{aligned} \tag{4b}$$

In Eq. (3),

$$p_{s0} = \rho(c_b r_p/r_d)^2/h \tag{4c}$$

is the static pressure in the constrained disk produced by a unit displacement at the footprint which accounts for the quasi-static uniform bulk pressure. The reason why the superposition in Eq. (3) is necessary is explained in what follows. Since the dynamic solution satisfies homogeneous boundary conditions, the only way that the forcing function of prescribed traction or displacement can be included in the problem is by adding the static solution multiplied by the time dependence of the forcing function [14].

The second boundary condition in Eq. (4b) is mixed: over one part of the boundary only the pressure gradient is prescribed while over the remaining boundary a combination of pressure and pressure gradient is prescribed. This difficulty can be overcome by the influence method [15]. The circle bounding the footprint is divided by $n+1$ equidistant radial stations with increment Δr_p:

$$0, r_1, r_2, \ldots, r_{n-1}, r_p, \quad r_k - r_{k-1} = \Delta r_p = \text{const.}$$

Assume a uniform pressure gradient of unit intensity to act over each annular segment $r_{k-1} \to r_k$, hereafter called the source segment. Evaluating the pressure gradient $P_{z,lk}(r,z;t)$ from the kth source segment at the center of the lth segment $r_{cl} = (r_l + r_{l-1})/2$, hereafter called the target point, and following the expansion in Eq. (3) yields

$$P_{z,lk}(r_{cl},0;t) = -p_{zs,lk}(r_{cl},0)\rho\ddot{f}_w(t) + p_{zd,lk}(r_{cl},0;t), \tag{5}$$

where $p_{zs,lk}(r_{cl},0)$ and $p_{zd,lk}(r_{cl},0)$ are static and dynamic pressure gradients at the lth target point due to the kth source segment. Enforcing the condition of prescribed pressure gradient $p_z(t) = p_{zf}(t)$ over the footprint at each time step yields a set of simultaneous equations in the weights $c_k(t)$:

$$\sum_{k=1}^{n} P_{z,lk}(r_{cl}, 0; t)c_k(t) = p_{zf}(t), \quad l = 1, n. \tag{6a}$$

The combined pressure from all annular source segments is the superposition of $P_{lk}(r, z; t)$ multiplied by time-dependent weights $c_k(t)$ as follows:

$$\begin{aligned} p(r, z; t) &= \sum_{k=1}^{n} P_{lk}(r, z; t)c_k(t), \quad l = 1, n, \\ P_{lk}(r, z; t) &= -p_{s,lk}(r, z)\rho\ddot{f}_w(t) + p_{d,lk}(r, z; t). \end{aligned} \tag{6b}$$

Solutions of $p_{s,k}(r, z; t)$ and $p_{d,k}(r, z; t)$ for each unit source segment are outlined in what follows. The static solution due to the kth source segment takes the form

$$p_{s,k}(r, z) = \sum_{m=1}^{m_r} \psi_{sm,k}(z)J_0(k_{rm}r), \quad \psi_{sm,k}(z) = \alpha_{mk}\sinh(k_{rm}z) + \beta_{mk}\cosh(k_{rm}z), \tag{7}$$

where $J_0(k_{rm}r)$ is the Bessel function and $1 \leqslant m \leqslant m_r$ is a truncated number of radial wavenumbers m in the expansion. Substituting Eq. (7) in the boundary conditions

$$\begin{aligned} &\partial_r p_{s,k}(r_d, z) + Y_r p_{s,k}(r_d, z) = 0, \\ &\partial_z p_{s,k}(r, 0) - Y_z p_{s,k}(r, 0) = -(H(r - r_{k-1}) - H(r - r_k)), \\ &\partial_z p_{s,k}(r, h) + Y_z p_{s,k}(r, h) = 0 \end{aligned} \tag{8}$$

and enforcing orthogonality of $J_0(k_{rm}r)$ yields

$$\begin{aligned} &k_{rm}J_1(k_{rm}r_d) - Y_r J_0(k_{rm}r_d) = 0, \quad m = 1, m_r, \\ &\alpha_{m,k} = \frac{2(r_k J_1(k_{rm}r_k) - r_{k-1}J_1(k_{rm}r_{k-1}))}{r_d^2 J_0^2(k_{rm}r_d)(k_{rm} + Y_z\eta_m)}, \quad \beta_{m,k} = -\alpha_{m,k}\eta_m, \\ &\eta_m = \frac{k_{rm} + Y_z\tanh(k_{r\,m}\,h)}{k_{rm}\tanh(k_{rm}h) + Y_z}. \end{aligned} \tag{9}$$

Note that in Eq. (5), $p_{zs,lk}(r_{cl}, 0) = \partial_z p_{s,k}(r_{cl}, 0)$.

The dynamic solution $p_{d,k}(r, z; t)$ satisfies

$$\nabla_0^2 p_{d,k} - \frac{1}{c_b^2}\partial_{tt}p_{d,k} = 0 \tag{10a}$$

and the homogeneous boundary conditions

$$\begin{aligned} &\partial_r p_{d,k}(r_d, z; t) + Y_r p_{d,k}(r_d, z; t) = 0, \\ &\partial_z p_{d,k}(r, 0; t) - Y_z p_{d,k}(r, 0; t) = 0, \\ &\partial_z p_{d,k}(r, h; t) + Y_z p_{d,k}(r, h; t) = 0. \end{aligned} \tag{10b}$$

Expand $p_{d,k}(r, z; t)$ in terms of its eigenfunctions

$$p_{d,k}(r, z; t) = \sum_m \sum_n a_{mn,k}(t)\,\psi_{dn}(z)\,J_0(k_{rm}r). \tag{11a}$$

Applying the homogeneous boundary conditions in Eq. (10b) to $J_0(k_{rm}r)$ and $\psi_{dn}(z)$ produces the dispersion relations

$$k_{rm}J_1(k_{rm}r_d) - Y_r J_0(k_{rm}r_d) = 0, \quad m = 1, m_r, \tag{11b}$$

$$\sin(k_{zn}h) - \zeta_n(\zeta_n\sin(k_{zn}h) + 2\cos(k_{zn}h)) = 0, \quad n = 1, n_z, \tag{11c}$$

$$\psi_{dn}(z) = \cos(k_{zn}z) + \zeta_n \sin(k_{zn}z), \quad \zeta_n = Y_z/k_{zn},$$
$$\omega_{mn} = c_b k_{mn} = c_b\sqrt{k_{zn}^2 + k_{rm}^2}, \tag{11d}$$

where ω_{mn} is the eigenvalue corresponding to mode (m,n), k_{rm} is the mth root of the dispersion relation (11b), and k_{zn} is the nth root of the dispersion relation (11c). If $Y_r = Y_z = 0$, $k_{zn} = 0$ is the only root of Eq. (11c). Substituting Eq. (3) in Eq. (2) with use made of Eq. (7) and (11a) and enforcing orthogonality of $\psi_{dn}(z)$ and $J_0(k_{rm}r)$ yields

$$\ddot{a}_{mn,k}(t) + \omega_{mn}^2 a_{mn,k}(t) = -N_{sdmn,k} \quad \rho f_w^{iv}(t),$$
$$N_{sdmn,k} = \frac{1}{N_{zzn}}\int_0^h \psi_{sm,k}(z)\psi_{dn}(z)\,\mathrm{d}z, \quad m = 1, m_r, \quad n = 1, n_z,$$
$$N_{zzn} = \frac{Y_z}{2k_{zn}^2}(1-\cos(2k_{zn}h)) + \frac{1}{4k_{zn}}(1-Y_z^2/k_{zn}^2)\sin(2k_{zn}h) + \frac{h}{2}(1+Y_z^2/k_{zn}^2). \tag{12}$$

$(\,)^{iv}$ is the fourth derivative with respect to time. The solution to Eq. (12) is expressed as a Duhamel integral:

$$a_{mn,k}(t) = -\frac{\rho N_{sdmn,k}}{\omega_{mn}}\int_0^t \sin\omega_{mn}(t-\tau) f_w^{iv}(\tau)\,\mathrm{d}\tau. \tag{13}$$

Once the $a_{mn,k}(t)$ are determined for each time step, then $p_{d,k}(r,z,t)$ and its gradient $p_{zd,k}(r,z,t)$ follow from Eq. (11a). Finally, substituting $p_{zd,k}(r_{cl},0,t)$ and $p_{zs,k}(r_{cl},0)$ from Eq. (7) in Eq. (5) yields the influence coefficients $P_{z,lk}(r_{cl},0;t)$ determining the weights $c_k(t)$ from Eq. (6a) and thus the transient pressure from Eq. (6b). Acoustic displacements (w,u) are calculated from

$$\partial_z p_{d,k} = -\rho\,\partial_{tt}^2 w_k, \quad \partial_r p_{d,k} = -\rho\partial_{tt}^2 u_k. \tag{14}$$

Note that in Eq. (14), $\partial_z p_{d,k}(r_{cl},0;t) \equiv p_{zd,lk}(r_{cl},0;t)$ as defined in Eq. (5). Once histories of $\partial_z p_{d,k}$ and $\partial_r p_{d,k}$ are determined from solving Eq. (13), histories of w_k and u_k are calculated by integrating Eq. (14) numerically.

3. Results

Static solutions of a constrained layer adopting modal analysis and finite difference are compared first. In order to re-use mobilities calculated in Ref. [16], material properties and geometry must be the same as in that reference. Therefore, the geometry and material properties of the layer are

$$h = 0.5\,\text{in}(=1.27\,\text{cm}), \quad r_d = 2\,\text{in}(=5.08\,\text{cm}),$$
$$r_p = 0.375\,\text{in}(=0.95\,\text{cm}),$$
$$c_b = 4\times10^5\,\text{in/s}(=10.16\,\text{km/s}),$$
$$\rho = 3\times10^{-4}\,lb\,\text{s}^2/\text{in}^4(=3.21\,\text{g/cm}^3). \tag{15}$$

Two wall conditions are considered: rigid wall and compliant wall with $Y_r = 5\,\text{in}^{-1}(=1.97\,\text{cm}^{-1})$ and $Y_z = 5\,\text{in}^{-1}(=1.97\,\text{cm}^{-1})$ [16]. Fig. 1 compares distributions of $p_s(r,z_o)$, $\partial_z p_s(r,z_o)$ and $\partial_r p_s(r,z_o)$ computed by the two methods for the compliant boundary at five equidistant stations along z; $z = 0$, $0.25h$, $0.5h$, $0.75h$, h where the origin of (r,z) is at the center of the footprint. Fig. 1(b1,b2) reproduce the constraint $\partial_z p_s(r,0) = -(H(r) - H(r-r_p))$. Both $\partial_z p_s(r,0)$ and $\partial_r p_s(r,0)$ are discontinuous along the perimeter of the footprint $r = r_p$ as prescribed by boundary condition (4b). $p_s(r,z_o)$ is bell-shaped and can be approximated by $p(r) = p_0 + p_1\sec h(p_2 r)$. Results from the two methods agree except for relatively small oscillations owing to the truncation set by m_r.

For the transient problem, Fig. 2 plots prescribed motion $\ddot{f}_w(t)$, $\dot{f}_w(t)$ and $f_w(t)$ at the footprint. $\ddot{f}_w(t)$ is made of 6 linear segments for this example:

1. Linear acceleration : $\ddot{f}_{w1}(t) = \alpha_1 t, \quad 0 \leqslant t \leqslant t_1.$
2. Constant acceleration : $\ddot{f}_{w2}(t) = \alpha_1 t_1, \quad t_1 \leqslant t \leqslant t_2.$
3. Linear deceleration : $\ddot{f}_{w3}(t) = \ddot{f}_{w2}(t_2) - \alpha_2(t - t_2), \quad t_2 \leqslant t \leqslant t_3.$

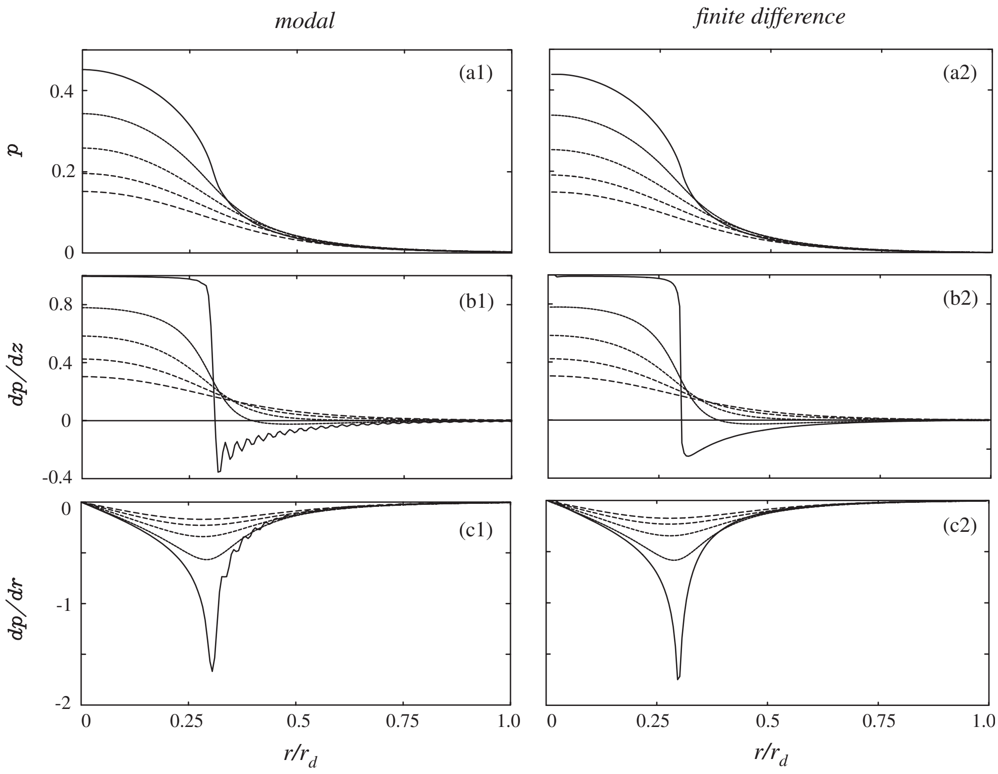

Fig. 1. Static solution in cavity with compliant boundaries: $Y_r = Y_z = 5\,\mathrm{in}^{-1}$; (a1), (b1), (c1) modal; (a2), (b2), (c2) finite difference:—, $z/h0$; -------, $z/h0.25$; ----, $z/h = 0.5$;---$z/h = 0.75$; ---, $z/h = 1$.

4. Constant velocity : $\ddot{f}_{w4}(t) = 0, \quad \dot{f}_{w4}(t_3) = V_0, \quad t_3 \leqslant t \leqslant t_4.$
5. Linear deceleration : $\ddot{f}_{w5}(t) = -\alpha_3(t - t_4), \quad t_4 \leqslant t \leqslant t_5.$
6. Constant deceleration : $\ddot{f}_{w6}(t) = -\alpha_3(t_5 - t_4), \quad t_5 \leqslant t \leqslant t_6.$

Assuming that the first three time intervals are equal ($\Delta t_1 = \Delta t_2 = \Delta t_3$, $\Delta t_i = t_i - t_{i-1}$) and $\alpha_2 = \alpha_1$, then α_1 is determined by prescribing the constant velocity $\dot{f}_{w4}(t_3) = U_0$. Also, setting α_{3}/α_2 to a known constant determines t_6 when the velocity vanishes. In this example, parameters defining $\ddot{f}_w(t)$ are

$$\begin{aligned} &\Delta t_{1,3} \equiv \Delta t_1 + \Delta t_2 + \Delta t_3 = 2\,\mu\mathrm{s}, \quad \Delta t_4 = 8\,\mu\mathrm{s}, \Delta t_5 = 8\,\mu\mathrm{s}, \\ &\alpha_3/\alpha_2 = 1/15, \quad U_0 = 2000\,\mathrm{ft/s}(= 609\,\mathrm{m/s}). \end{aligned} \tag{16}$$

Histories of $p(r, z_0; t)$ for the case with rigid boundaries $Y_r = Y_z = 0$ are plotted in Fig. 3(a1,b1) according to modal analysis and in Fig. 3(a2,b2) according to finite difference. Each Figure superimposes histories at $r = 0$, r_p, $2r_p$. Comparing Fig. 3(a1,b1)–(a2,b2) shows that results from the two methods agree. For $z = 0$ (Fig. 3(a1)), the peak pressure of first arrival at $r = 0$ is three times larger than that at $r = 2r_p$. This difference diminishes for $t > 4\,\mu\mathrm{s}$ as pressure homogenizes along r. The succeeding peak which starts appearing at $t = 10\,\mu\mathrm{s}$ is caused by reflections at the axis and lateral boundary. A mathematically equivalent description of the reflections from the axis that may be preferable from the physical standpoint is that waves propagate symmetrically from diametrically opposed directions. For the case with rigid boundaries, the average long-time response pressure rises with time following the rise of the quasi-static $p_{s0} f_w(t)$ in Eq. (4c) where $f_w(t)$ is the instantaneous displacement at the footprint (Fig. 2(c)). As z increases (Fig. 3(b1)), the peak pressure of first arrival diminishes yet succeeding peaks are insensitive to z.

Fig. 4(a–d) plot the instantaneous distribution of $p(r, z_0; t_0)$ along r at $z_0 = 0$ and $z_0 = h$. At $t_0 = 1.5\,\mu\mathrm{s}$ soon after start of motion (Fig. 4(a)), $p(r, 0; t_0)$ reaches its peak following a bell-shaped distribution. For $t_0 = 2.5\,\mu\mathrm{s}$ (Fig. 4(b)), $p(r, h; t_0)$ reaches its peak while $p(r, 0; t_0)$ diminishes. At $t_0 = 3.5\,\mu\mathrm{s}$ (Fig. 4(c)), pressure continues

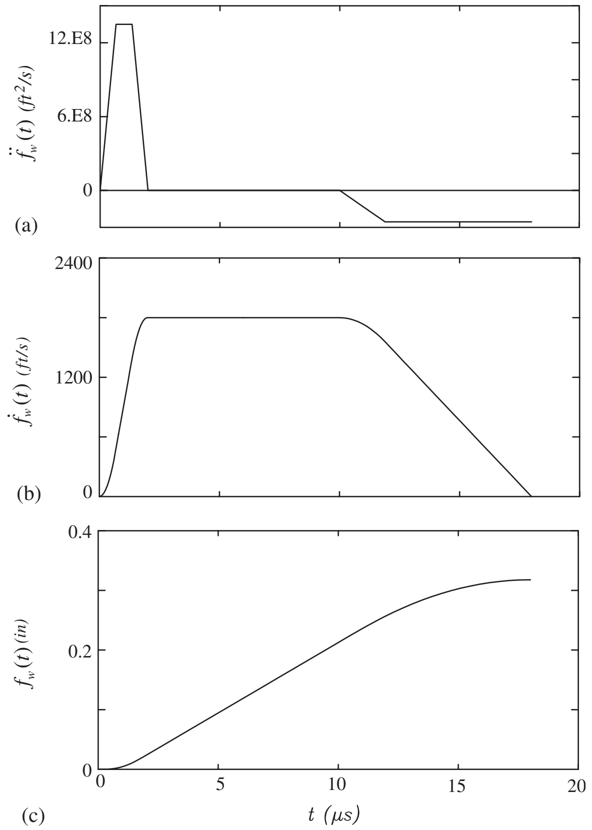

Fig. 2. Prescribed motion at footprint: (a) acceleration, (b) velocity, (c) displacement.

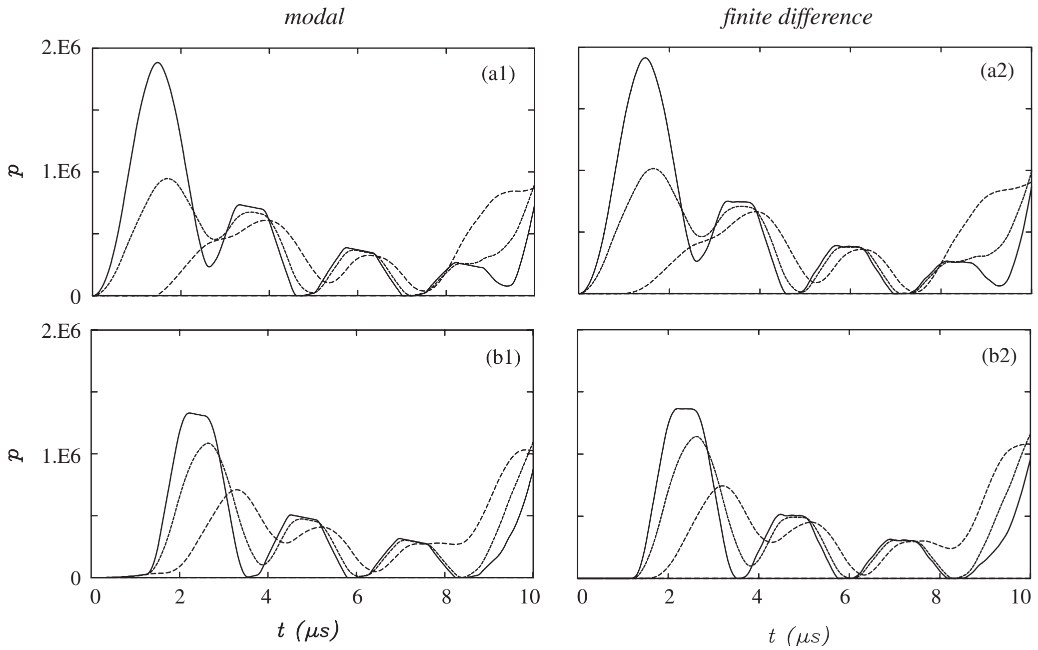

Fig. 3. Pressure histories in cavity with rigid boundaries: $Y_r = Y_z = 0$, $\Delta t_{13} = 2\,\mu\text{s}$, $U_0 = 2000\,\text{ft/s}$ (al), (b1) modal: (a2), (b2) finite difference. — $r = 0$; -----, $r = r_p$;- - - -, $r = 2r_p$. (a1) and (a2): $z = 0$; (b1) and (b2): $z = h$.

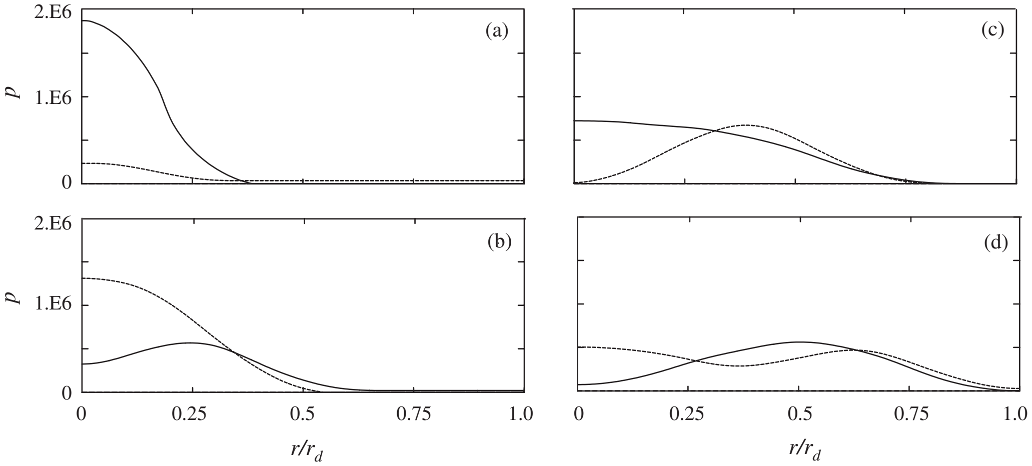

Fig. 4. Instantaneous $p(r;z_0;t_0)$ distribution in cavity with rigid boundaries, $\Delta t_{13} = 2\,\mu s$, $U_0 = 2000\,\mathrm{ft/s}$, —, $z_0 = h$;- - - -, $z_0 = 0$. (a) $t_0 = 1.5\,\mu s$, (b) $2.5\,\mu s$, (c)$3.5\,\mu s$, (d) $4.5\,\mu s$.

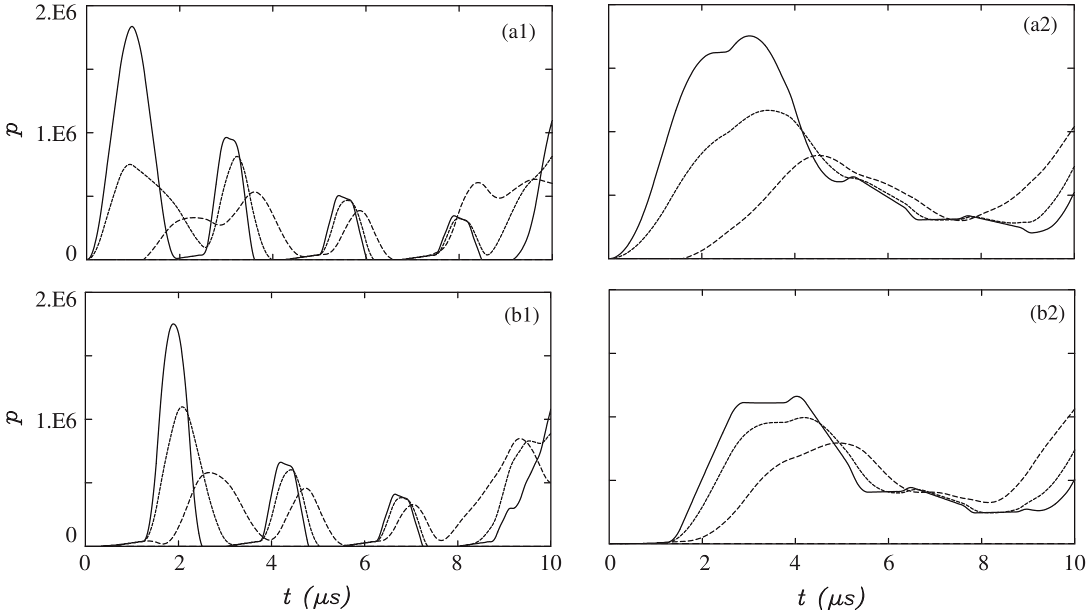

Fig. 5. Effect of $\Delta t_{1,3}$ and U_0 on histories in cavity with rigid boundaries. (al), (b1) $\Delta t_{1,3} = 1\,\mu s$, $U_0 = 1300\,\mathrm{ft/s}$; (a2), (b2) $\Delta t_{1,3} = 4\,\mu s$, $U_0 = 3300\,\mathrm{ft/s}$. $r = 0$; - - - -, $r = r_p$ ———, $r = 2r_p$. (a1) and (a2): $z = 0$; (b1) and (b2): $z = h$.

both to homogenize and to decrease till the wave front reaches the lateral boundary $r = r_d$ at $t_0 = 4.5\,\mu s$ (Fig. 4(d)). Pressure rises after each reflection from the lateral boundary and axis.

The sensitivity to parameters $\Delta t_{1,3}$ and U_0 of pressure response is demonstrated in Fig. 5. For $\Delta t_{1,3} = 1\,\mu s$ and $U_0 = 1300\,\mathrm{ft/s}(= 396\,\mathrm{m/s})$, histories are shown in Fig. 5(a1,b1). Comparing Fig. 5(a1) and 3(a1) shows that at the footprint, a shorter $\Delta t_{1,3}$ compensates for a lower U_0 yielding a narrower peak with the same magnitude and width proportional to $\Delta t_{1,3}$. However, this does not apply at $z = h$ where a shorter $\Delta t_{1,3}$ yields a stronger peak despite the difference in U_0 (Fig. 5(b1)). For $\Delta t_{1,3} = 4\,\mu s$ and $U_0 = 3200\,\mathrm{ft/s}(= 975\,\mathrm{m/s})$ (Fig. 5(a2) and (b2)) the same phenomenon is observed at the footprint; that is a higher U_0 compensates for the longer $\Delta t_{1,3}$ yielding a wider peak with the same magnitude as evidenced by comparing Figs. 5(b1) and

3(b1). Consistent with the way $\Delta t_{1,3}$ affects peak pressure remote from the footprint, comparing Figs. 5(b2), 3(b1) and 5(b1) show that a longer $\Delta t_{1,3}$ yields a weaker and wider peak.

Fig. 6 plots $p_{\max}$ against U_0 with $\Delta t_{1,3}$ held fixed and vice versa. Fig. 6(a1) and (a2) shows that $p_{\max}$ varies linearly with U_0. Fig. 6(b1) and (b2) shows that $p_{\max}$ varies nonlinearly with $\Delta t_{1,3}$ following the relation $p_{\max} \propto U_0 \Delta t_{13}^{-\alpha}$, where the exponent α depends on z. $p_{\max}$ asymptotes to a constant value as $\Delta t_{1,3} \to 0$ when the slope of the acceleration profile in Fig. 2(a) approaches infinity. For $\Delta t_{1,3} < 1$, dependence of $p_{\max}$ on $\Delta t_{1,3}$ undergoes a transition when its value at $z = h$ exceeds that at the footprint $z = 0$. Fig. 7(a) and (b) plots pressure histories at $z = 0$ and $z = h$ for $U_0 = 1600$ ft/s(= 488 m/s) and two values of $\Delta t_{1,3}$ lying on each side of the transition. Fig. 7(a1) shows that at $\Delta t_{1,3} = 0.2\,\mu$s, the pressure over the footprint is trapezoidal lasting 1 μs which is $\approx 5\Delta t_{1,3}$. In Fig. 7(a1), the second peak originating from reflection at $z = h$ has twice the amplitude and width $\approx 2\Delta t_{1,3}$. Fig. 7(b1) shows that at $z = h$ peak of first arrival is 2.2 times higher than footprint pressure consistent with its value after reflection appearing as the second peak in Fig. 7(a1). Fig. 7(a2) shows that at $\Delta t_{1,3} \leqslant (\Delta t_{1,3})_T = 1\,\mu$s footprint pressure reverts to being the highest with the familiar bell-shaped response. This also applies to the peak of first arrival at $z = h$ shown in Fig. 7(b2). $(\Delta t_{1,3})_T$ is a function of E_b and ρ but is almost independent of U_0.

The effect of boundary compliance on pressure response is shown in Fig. 8(a) and (b) with U_0 and $\Delta t_{1,3}$ the same as those of Fig. 3. Mobilities of the radial and axial boundaries are set to $Y_r = Y_z = 5\,\text{in}^{-1}(= 1.97\,\text{cm}^{-1})$ [16]. Comparing pressure histories in Figs. 3(a1) and 8(a) reveal that the magnitude of footprint pressure remains the same since it is not affected by the neighboring boundary. However, at $t = 10\,\mu$s, pressure reflected from the radial boundary $r = r_d$ is reduced substantially by wall compliance. At $z = h$, the peak pressure of first arrival (Fig. 8(b)) is half that for the case with rigid boundaries (Fig. 3(b1)) while the response following that peak is attenuated. Instantaneous pressure profiles along r are shown in Fig. 9(a–c). Comparing profiles in Fig. 9(b) to those for rigid walls in Fig. 4(b) shows how pressure is reduced due to boundary compliance. Also, comparing profiles in Fig. 9(c) to those in Fig. 3(c) shows how compliance attenuates response following the first peak.

Numerical results by the EPIC2 general purpose finite difference program were determined for the following example [17]: (1) ceramic disk 1/2″(= 1.27 cm) thick and 2″(= 5.08 cm) in diameter ; (2) tungsten capsule 1/4″(= 0.635 cm) thick; (3) steel cylindrical projectile 1.5″(= 3.81 cm) long and 0.75”(1.91 cm) in diameter striking at 2300 ft/s (= 701 m/s).

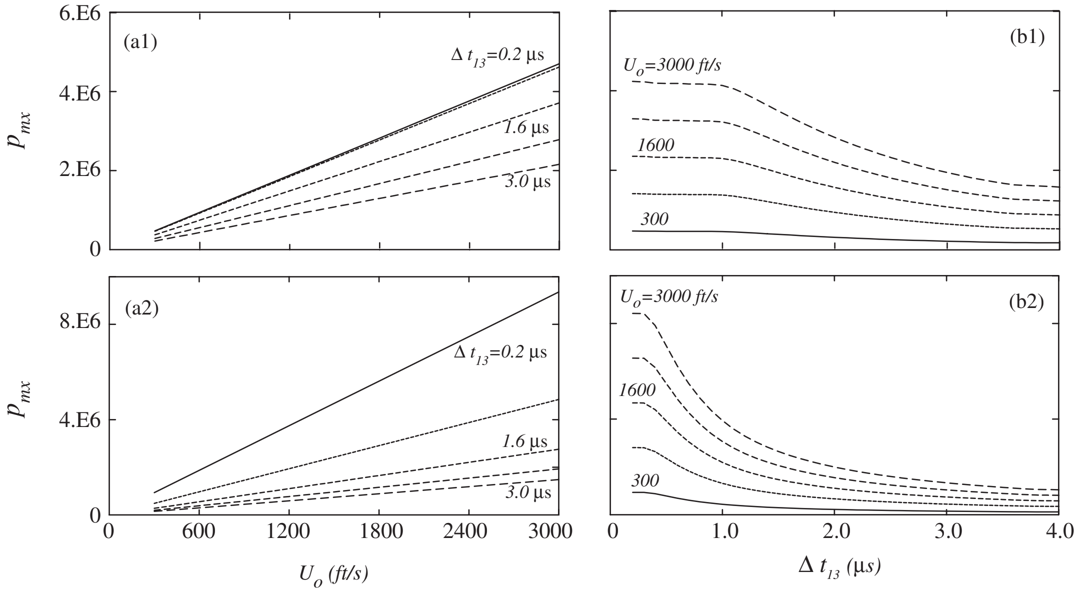

Fig. 6. Variation of $p_{\max}$. with U_0 and $\Delta t_{1,3}$ in a cavity with rigid boundaries. (a1), (bl) $z = 0$, (a2), (b2) $z = h$.

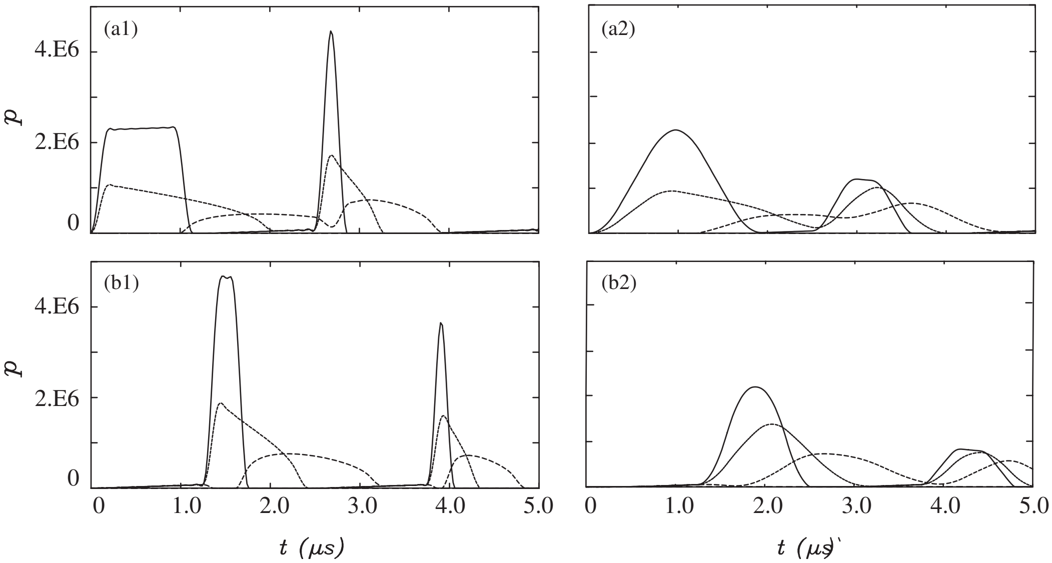

Fig. 7. Pressure histories for small $\Delta t_{1,3}$ in a cavity with rigid boundaries. (a1), (bl) $\Delta t_{13} = 0.2\,\mu\text{s}$, (a2), (b2) $\Delta t_{13} = 1.0\,\mu\text{s}$. — $r = 0$; - - - -, $r = r_p$; ———, $r = 2r_p$; $U_0 = 1600\,\text{ft/s}$.

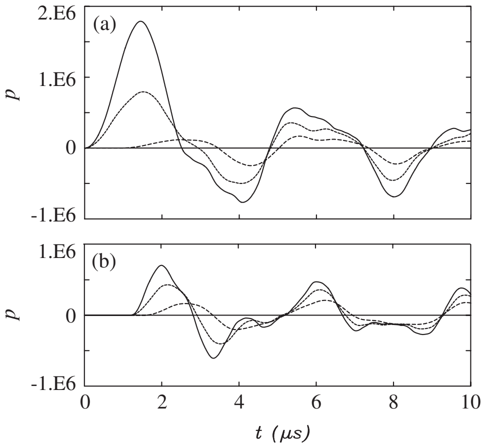

Fig. 8. Pressure histories in cavity with compliant boundaries: $Y_r = Y_z = 5\,\text{in}^{-1}$, $\Delta t_{13} = 2\,\mu\text{s}$ $U_0 = 2000\,\text{ft/s}$, (a) $z = 0$, (b) $z = h$. — $r = 0$; - - - - -, $r = r_p$; - - - - -, $r = 2r_p$.

Fig. 10 compares pressure histories on the top and bottom faces of the ceramic disk with those from the acoustic model with compliant boundaries. Wall dynamic mobility was determined from an analytical elastodynamic model of the capsule developed in Ref. [16]. Since failed ceramic does not resist tensile stress, only compressive stress is shown in the acoustic histories. At $z = 0$ and h, the pulse of first arrival from the two models compares favorably both in magnitude and shape. Reflected peaks do not agree as well since the EPIC results decay rapidly from artificial viscosity necessary to stabilize the numerical calculations. Fig. 11 compares time snap-shots of pressure distribution along r predicted by the acoustic model and those from EPIC2. The $0.5\,\mu\text{s}$ lag between corresponding snap-shots of EPIC2 and the acoustic models allows for the propagation time of the wave starting impact across the capsule's top plate. In spite of the limited number of points in the EPIC2 results, comparison is favorable.

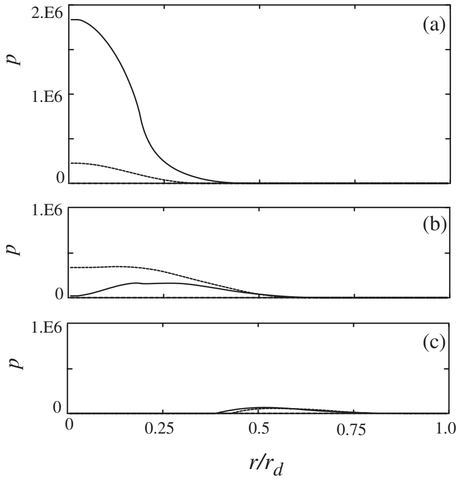

Fig. 9. Instantaneous $p(r;z_0;t_0)$ distribution in cavity with compliant boundaries: $Y_r = Y_z = 5\,\text{in}^{-1}$, $\Delta t_{1,3} = 2\,\mu\text{s}$ $U_0 = 2000\,\text{ft/s}$, (a) $t = 1.5\,\mu\text{s}$, (b) $2.5\,\mu\text{s}$, (c) $3.5\,\mu\text{s}$.

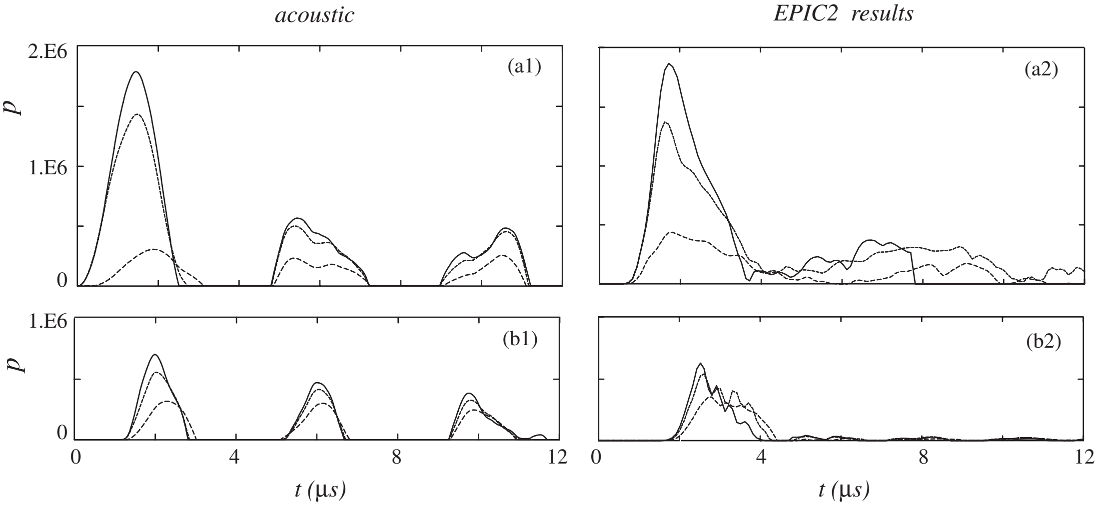

Fig. 10. Comparison of acoustic and numerical pressure histories: —, $r = 0$; - - - - -, $r = 0.25''$; - - - - -$r = 0.5''$. (a1), (b1) acoustic model with complient boundaries, (a2), (b2) EPIC results. (a1) and (a2): $z = 0$; (b1) and (b2): $z = h$.

4. Conclusion

Pressure generated from impact on the mass of confined comminuted material is modeled by the acoustic wave equation that derives from the elasto-dynamic equations when shear stress vanishes. The transient response from prescribed acceleration at the boundary is treated adopting both a modal and a finite difference approach. In the modal approach, external excitation is modeled by the static-dynamic superposition method. The difficulty of mixing boundary conditions from finite wall compliance is overcome by the influence method. Noteworthy results are:

(1) Histories from the modal and finite difference approaches agree, justifying the linear acoustic treatment.
(2) Rise time in pressure history is proportional to $\Delta t_{1,3}$ while $p_{\max}$ is proportional to $U_0 \Delta t_{13}^{-\alpha}$.
(3) For $\Delta t_{1,3} < (\Delta t_{1,3})_T$, $p_{\max}$ goes through a transition when its value at face $z = h$ exceeds that at the footprint $z = 0$. $(\Delta t_{1,3})_T$ is a function of E_b and ρ but is almost independent of U_0.

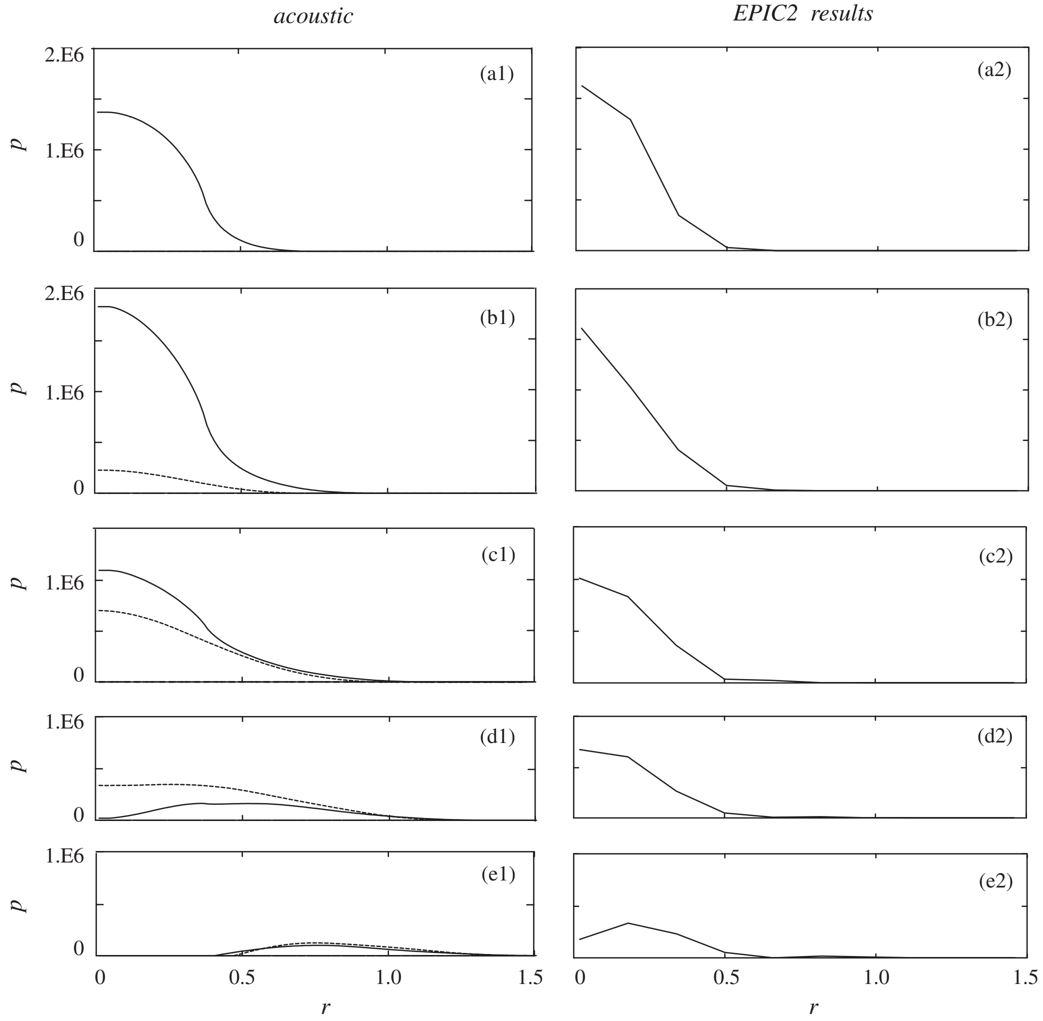

Fig. 11. Comparison of $p(r; z_0)$ snap-shots from acoustic and numerical models: (a1)–(el) acoustic model with complient boundaries, (a2)–(e2) EPIC results. —, $z/h = 0$; - - - - -, $z/h = 1$. (a1) $t = 1\,\mu s$, (b1) $1.5\,\mu s$, (c1) $2\,\mu s$, (d1) $2.5\,\mu s$, (e1) $3\,\mu s$; (a2) $t = 1.5\,\mu s$, (b2) $2\,\mu s$, (c2) $2.5\,\mu s$, (d2) $3\,\mu s$, (e2) $3.5\,\mu s$.

(4) Wall compliance reduces pressure peaks of first arrival everywhere except at the footprint.
(5) Histories and pressure snap-shots of the acoustic model agree with results of the EPIC2 computer program implying that locally, confined comminuted material behaves indeed like a fluid.

Appendix A. Finite difference formulation

Consider the axisymmetric acoustic equation in cylindrical coordinates:

$$[\partial_{rr} + 1/r\partial_r + \partial_{zz}]p(r, z; t) = 1/c_b^2 \partial_{tt} p(r, z; t) \tag{A.1}$$

with boundary conditions

$$\partial_r p(0, z; t) = 0, \tag{A.2a}$$

$$\partial_r p(r_d, z; t) + Y_r p(r_d, z; t) = 0, \tag{A.2b}$$

$$\partial_z p(r,0;t) - Y_z p(r,0;t) = 0, \tag{A.2c}$$

$$\partial_z p(r,h;t) = \begin{cases} -\rho \ddot{f}_w(t)[H(r) - H(r-r_p)], & 0 \leqslant r \leqslant r_p, \\ -Y_z p(r,h;t), & r_p < r \leqslant r_d, \end{cases} \tag{A.2d}$$

where ($\dot{}$) is time derivative and letting z now have its origin at the non-excited boundary. Condition (A.2a) is symmetry about the axis of revolution $r = 0$, condition (A.2b) is the resilient boundary at $r = r_d$, condition (A.2c) is the resilient boundary at $z = 0$, and condition (A.2d) is the prescribed acceleration for $0 \leqslant r \leqslant r_p$ and resilient boundary for $r_p \leqslant r \leqslant r_d$ at $z = h$.

Form the rectangular grid with nodes along r and z denoted by i and j, respectively:

$$\begin{aligned} &i = 1 \to n_r, d_r \leqslant r \leqslant r_d - d_r, d_r = r_d/(n_r + 1), \\ &j = 1 \to n_z, d_z \leqslant z \leqslant h - d_z, d_z = h/(n_z + 1). \end{aligned} \tag{A.3}$$

In this grid, nodes do not include points on the boundaries. Expressing Eq. (A.1) in central difference to first order yields the following relations depending on position:

(1) Internal points $d_r < r < r_d - d_r,\ d_z < z < h - d_z \Rightarrow 2 \leqslant i \leqslant n_r - 1,\ 2 \leqslant j \leqslant n_z - 1,$

$$\begin{aligned} &\alpha_1 p_{i+1,j} + \alpha_2 p_{i-1,j} + \alpha_3 p_{i,j} + \alpha_4 (p_{i,j+1} + p_{i,j-1}) = \ddot{p}_{i,j}/c_b^2, \\ &\alpha_1 = \left(\frac{1}{d_r^2} + \frac{1}{2r_i d_r}\right), \alpha_2 = \left(\frac{1}{d_r^2} - \frac{1}{2r_i d_r}\right), \\ &\alpha_3 = -2\left(\frac{1}{d_r^2} + \frac{1}{d_z^2}\right), \alpha_4 = \frac{1}{d_z^2}. \end{aligned} \tag{A.4a}$$

(2) Corner point $r = d_r, z = d_z \Rightarrow i = 1, j = 1,$

$$\alpha_1 p_{i+1,j} + (\alpha_2 + \alpha_3 + \alpha_4(1 - Y_z d_z)) p_{i,j} + \alpha_4 p_{i,j+1} = \ddot{p}_{i,j}/c_b^2. \tag{A.4b}$$

(3) Points along axis $r = d_r, d_z < z < h - d_z \Rightarrow i = 1, 2 \leqslant j \leqslant n_z - 1,$

$$\alpha_1 p_{i+1,j} + (\alpha_2 + \alpha_3) p_{i,j} + \alpha_4 (p_{i,j+1} + p_{i,j-1}) = \ddot{p}_{i,j}/c_b^2. \tag{A.4c}$$

(4) Corner point $r = r_d, z = h - d_z \Rightarrow i = 1, j = n_z,$

$$\begin{aligned} &\alpha_1 p_{i+1,j} + (\alpha_2 + \alpha_3 + \alpha_4(1 - Y_z d_z)) p_{i,j} + \alpha_4 p_{i,j-1} \\ &\quad = \ddot{p}_{i,j}/c_b^2 + \rho \ddot{f}_w(t)[H(r) - H(r - r_p)]/d_z. \end{aligned} \tag{A.4d}$$

(5) Points along $d_r < r < r_d - d_r, z = d_z \Rightarrow 2 \leqslant i \leqslant n_r - 1,\ j = 1,$

$$\alpha_1 p_{i+1,j} + \alpha_2 p_{i-1,j} + (\alpha_3 + \alpha_4(1 - Y_z d_z)) p_{i,j} + \alpha_4 p_{i,j+1} = \ddot{p}_{i,j}/c_b^2. \tag{A.4e}$$

(6) Points along $d_r < r < r_d - d_r,\ z = h - d_z \Rightarrow 2 \leqslant i \leqslant n_r - 1, j = n_z,$

$$\begin{aligned} &\alpha_1 p_{i+1,j} + \alpha_2 p_{i-1,j} + (\alpha_3 + \alpha_4) p_{i,j} + \alpha_4 p_{i,j-1} \\ &\quad = \ddot{p}_{i,j}/c_b^2 + \rho \ddot{f}_w(t)/d_z, \quad d_r < r \leqslant r_p, \\ &\alpha_1 p_{i+1,j} + \alpha_2 p_{i-1,j} + (\alpha_3 + \alpha_4(1 - Y_z d_z)) p_{i,j} + \alpha_4 p_{i,j-1} \\ &\quad = \ddot{p}_{i,j}/c_b^2, \quad r_p < r \leq r_d - d_r. \end{aligned} \tag{A.4f}$$

(7) Corner point $r = r_d - d_r,\ z = d_z \Rightarrow i = n_r, j = 1,$

$$\alpha_2 p_{i-1,j} + (\alpha_1(1 - Y_r d_r) + \alpha_3 + \alpha_4(1 - Y_z d_z)) p_{i,j} + \alpha_4 p_{i,j+1} = \ddot{p}_{i,j}/c_b^2. \tag{A.4g}$$

(8) Points along $r = r_d - d_r, d_z < z < h - d_z \Rightarrow i = n_r, 2 \leqslant j \leqslant n_z - 1$,

$$\alpha_2 p_{i-1,j} + (\alpha_1(1 - Y_r d_r) + \alpha_3)p_{i,j} + \alpha_4(p_{i,j+1} + p_{i,j-1}) = \ddot{p}_{i,j}/c_b^2. \tag{A.4h}$$

(9) Corner point $r = r_d - d_r,\ z = h - d_z \Rightarrow i = n_r,\ j = n_z$,

$$\alpha_2 p_{i-1,j} + (\alpha_1(1 - Y_r d_r) + \alpha_3 + \alpha_4(1 - Y_z d_z))p_{i,j} + \alpha_4 p_{i,j-1} = \ddot{p}_{i,j}/c_b^2. \tag{A.4i}$$

In Eq. (A.4a)–(A.4i), the differential equation is satisfied at all points in the grid and boundary conditions are enforced at points along its perimeter. In terms of finite difference, Eq. (A.2d) takes the form

$$p_{i,j+1} = p_{i,j} - \rho d_z \ddot{f}_w(t)[H(r) - H(r - r_p)], 1 \leqslant i \leqslant \mathrm{int}(r_p/d_r), \quad j = n_z. \tag{A.5}$$

In Eq. (A.5), $\rho d_z \ddot{f}_w(t)[H(r) - H(r - r_p)]/d_z^2$ is the forcing term appearing on the right hand side of Eqs. (A.4d) and (A.4f).

Applying Eqs. (A.4a)–(A.4i) at all internal points in the grid (A.3) produces a set of ordinary differential equations in $p_{i,j}(t)$ cast in the form of tri-diagonal blocks as

$$\ddot{\mathbf{p}} = c_b^2(\mathbf{M}_p\mathbf{p} - \mathbf{F}(t)), \tag{A.6}$$

$$\mathbf{M}_p = \begin{bmatrix} \mathbf{A}_1 & \mathbf{C}_1 & & & \\ \mathbf{B}_2 & \mathbf{A}_2 & \mathbf{C}_2 & & \\ & \bullet & \bullet & \bullet & \\ & & \mathbf{B}_{n_r-1} & \mathbf{A}_{n_r-1} & \mathbf{C}_{n_r-1} \\ & & & \mathbf{B}_{n_r} & \mathbf{A}_{n_r} \end{bmatrix}.$$

$\mathbf{B}_i$ and $\mathbf{C}_i$ are $(n_z \times n_z)$ diagonal matrices, $\mathbf{A}_i$ is a $(n_z \times n_z)$ banded matrix with bandwidth 3, and $\mathbf{F}$ is the global vector of the forcing function in Eqs. (A.4d) and (A.4f). For each point $j \ni (1 \leqslant j \leqslant n_z)$ along an i line in the grid, coefficients of $p_{i,j}$ in the Laplacian define $\mathbf{A}_i$, coefficients of $p_{i-1,j}$ define $\mathbf{B}_i$, and coefficients of $p_{i+1,j}$ define $\mathbf{C}_i$. The time derivative is expressed in central difference to first order allowing integration in time.

Viscous damping is included following Landau and Lifshitz [18]:

$$(1 + 2\tilde{\nu}/c_b^2\partial_t)\nabla_0^2 p - 1/c_b^2\partial_{tt}p = 0. \tag{A.7}$$

This modifies Eq. (A.6) to the following first-order system:

$$\dot{\mathbf{p}} = \mathbf{q}, \dot{\mathbf{q}} = c_b^2\mathbf{M}_p\mathbf{p} + 2\tilde{\nu}\mathbf{M}_p\mathbf{q} - \mathbf{F}(t), \tag{A.8}$$

where $\tilde{\nu}$ is the equivalent of kinematic viscosity in a fluid. For sand, $\tilde{\nu} \approx 10^3\,\mathrm{in}^2/\mathrm{s}\,(= 6.45 \times 10^3\,\mathrm{cm}^2/\mathrm{s})$ which is 6 orders of magnitude larger than that of water.

References

[1] F. Theil, Young-measure solutions for a viscoelastically damped wave equation with nonmonotone stress–strain relation, *Archive for Rational Mechanics and Analysis* 144 (1) (1998) 47–78.

[2] H. Yserentant, A particle model of compressible fluids, *Numerische Mathematik* 76 (3) (1997) 111–142.

[3] H. Yserentant, The propagation of sound in particle models of compressible fluids, *Numerische Mathematik* 88 (3) (2001) 581–601.

[4] K. Sina, M. Khashayar, Analytical solution of wave equation for arbitrary non-homogeneous media, *Proceedings of SPI, The International Society of Optical Engineering* 4772 (2002) 25–36.

[5] R. Sujith, P. Subrahmanyam, P. Bala, T. Lieuwen, Propagation of sound in inhomogeneous media: exact solutions in curvilinear geometries, *Journal of Vibration and Acoustics, Transactions of the ASME* 125 (2) (2003) 133–136.

[6] S. Hamdi, W. Enright, W. Schiesser, J. Gottlieb, Exact solutions of the generalized equal width wave equation, *Lecture Notes in Computer Science* 266 (2003) 725–734.

[7] D. Yang, Grid modification for the wave equation with attenuation, *Numerische Mathematik* 67 (3) (1994) 391–401.

[8] J. Narayan, 2.5-D numerical simulation of acoustic wave propagation, *Pure and Applied Geophysics* 151 (1) (1998) 47–61.

[9] M. Scheman, F. Bornemann, An adaptive Rothe method for the wave equation, *Computing and Visualization in Science* 1 (3) (1998) 137–144.

[10] C. Bailly, D. Juve, Numerical solution of acoustic propagation problems using linearized Euler equations, *American Institute of Aeronautics and Astronautics Journal* 38 (1) (2001) 22–29.

[11] G. Wagner, M. Wenzel, W. Dumont, Numerical treatment of acoustic problems with the hybrid boundary element method, *International Journal of Solids and Structures* 38 (10–13) (2001) 1871–1888.

[12] L. Gaul, M. Wenzel, Acoustic calculations with the hybrid boundary element method in the time domain, *Engineering Analysis with Boundary Elements* 25 (4–5) (2001) 259–265.

[13] O. Mehdizadeh, M. Paraschivoiu, Investigation of a three-dimensional spectral element method for Helmholtz's Equation, *Lecture Notes in Computer Science* 2668 (2003) 819–825.

[14] J. Berry, P. Naghdi, On the vibration of elastic bodies having time dependent boundary conditions, *Quarterly of Applied Mathematics* 14 (1956) 43–50.

[15] M. El-Raheb, Wave propagation in a weak visco-elastic layer produced by prescribed velocity on the boundary, *Journal of Sound and Vibration* 275 (1–2) (2004) 89–106.

[16] M. El-Raheb, Transient response of a metallic capsule to an internal pressure pulse, *International Journal of Solids and Structures* 41/18–19 (2004) 4899–4918.

[17] T. Holmquist, G. Johnson, Modeling projectile impact into prestressed ceramic targets, *Proceedings of the Seventh International Conference on Mechanical and Physical Behavior of Materials Under Dynamic Loading* (2003).

[18] L. Landau, E. Lifshitz, *Fluid Mechanics*, first English edition, Pergamon Press, Addison-Wesley Publishing Company, Inc., Oxford, Reading, MA, 1959.